JOURNAL OF GEOPHYSICAL RESEARCH, VOL. 114, B08201, doi:10.1029/2008JB006018, 2009



# Measurement of the speed and attenuation of the Biot slow wave using a large ultrasonic transmitter

Youcef Bouzidi[1,2] and Douglas R. Schmitt[1]

Received 15 August 2008; revised 10 April 2009; accepted 21 May 2009; published 1 August 2009.

[1] Two compressional wave modes, a fast P1 and a slow P2, propagate through fluid-saturated porous and permeable media. This contribution focuses on new experimental tests of existing theories describing wave propagation in such media. Updated observations of this P2 mode are obtained through a water-loaded, porous sintered glass bead plate with a novel pair of ultrasonic transducers consisting of a large transmitter and a near-point receiver. The properties of the porous plate are measured in independent laboratory experiments. Waveforms are acquired as a function of the angle of incidence over the range from $-50^\circ$ to $+50^\circ$ with respect to the normal. The porous plate is fully characterized, and the physical properties are used to calculate the wave speeds and attenuations of the P1, the P2, and the shear S waves. Comparisons of theory and observation are further facilitated by numerically modeling the observed waveforms. This modeling method incorporates the frequency and angle of incidence-dependent reflectivity, transmissivity, and transducer edge effects; the modeled waveforms match well those observed. Taken together, this study provides further support for existing poroelastic bulk wave propagation and boundary condition theory. However, observed transmitted P1 and S mode amplitudes could not be adequately described unless the attenuation of the medium's frame was also included. The observed P2 amplitudes could be explained without any knowledge of the solid frame attenuation.

**Citation:** Bouzidi, Y., and D. R. Schmitt (2009), Measurement of the speed and attenuation of the Biot slow wave using a large ultrasonic transmitter, *J. Geophys. Res.*, *114*, B08201, doi:10.1029/2008JB006018.

## 1. Introduction

[2] It is now over 50 years since *Biot* [1956a, 1956b] predicted a second, or slow, compressional wave that exists in addition to the normal "fast" compressional and the shear waves in saturated porous and permeable media. It is nearly 30 years since *Plona* [1980] experimentally verified its existence. Despite this and also despite a large theoretical literature, there are still only a few definitive observations of the slow wave. The mode is highly attenuated; and it is not clear if it has yet been seen outside of the laboratory. However, our inability to find the slow wave directly does not mean that it does not affect overall seismic and sonar observations [e.g., *Allard et al.*, 1986; *Rasolofosaon*, 1988; *Pride et al.*, 2002; *Rubino et al.*, 2006]. Even if the slow wave is difficult to detect it still demands a portion of the total wavefield energy available; and it affects the amplitudes and phases of the more readily detectable compressional and shear waves transmitted through or reflected from a saturated formation. The degree to which the existence of the slow compressional wave influences seismic observations and the subsequent interpretations, which are made under the elastic paradigm, remains unclear; and continued study of such slow wave propagation is warranted.

[3] In this contribution we provide new experimental results of the transmission of waves through a well-characterized, saturated porous medium. The overall geometry of our experiments mimics those of *Plona* [1980] but with a newly developed ultrasonic transmitter-receiver pair that allows the transmitted amplitude time series to be recorded and analyzed with no correction permitting more accurate determination of both wave speed and attenuation [*Bouzidi and Schmitt*, 2006]. The reliability of the analysis is further supported by modeling of the full ultrasonic wavefield to account for the fact that the experiments were conducted not with hypothetical plane waves but with transducers of finite dimensions, these geometric effects are important particularly past critical angles where hypothetical plane wave behavior fails. Below, the background section first includes brief reviews of wave propagation phenomena in poroelasticity. The modified experimental acoustic goniometer, the manufacture and characterization of our artificial sample, and the data analysis strategy are then described. The observed wave forms transmitted through a water-saturated plate are presented, modeled, and interpreted, and compared to observations through a viscoelastic plate; and this contribution reiterates support for poroelastic theory. More importantly, however, it also prepares the way for the study

[1] Institute for Geophysical Research, Department of Physics, University of Alberta, Edmonton, Alberta, Canada.
[2] Now at Divestco Processing, Divestco Inc., Calgary, Alberta, Canada.


0148-0227/09/2008JB006018$09.00

of even more complex real rocks where other mechanisms are likely to be present.

## 2. Prior Work

[4] It is worth noting that many ultrasonic laboratory studies, while not describing an observation of the slow wave, have focused on the application of high-frequency *Biot* [1956b] theory to the normal fast longitudinal P1 wave [e.g., *Ogushwitz*, 1985; *Gist*, 1994a; *Williams et al.*, 2002; *Mayr and Burkhardt*, 2006; *Sebaa et al.*, 2006]. Many other studies [e.g., *Beamish et al.*, 1983; *Thomsen*, 1985; *Gist*, 1994b; *Mavko and Nolenhoeksema*, 1994; *King et al.*, 2000; *Han and Batzle*, 2004] attempt to reconcile laboratory studies with the low-frequency Biot-Gassmann limit [*Biot*, 1956a].

[5] Direct experimental observations of the slow P2 mode itself are still not common. *Smeulders* [2005] has recently provided a comprehensive review of this topic providing a history of possible observations of the slow wave and the early development of concepts prior to Biot's formulation and Plona's detection. *Plona* [1980] observed the P2 converted wave in a series of porous plates constructed by sintering glass beads. His capability to change the angle of incidence of the insonifying pulse allowed for observation of the converted P1, P2, and S modes at a variety of angles; this allowed him to convincingly argue that the P2 arrivals could not be experimental artifacts. This discovery led to a flurry of theoretical analyses of his P2 wave velocities [*Berryman*, 1980; *Dutta*, 1980] and transmitted amplitudes [*Hovem*, 1981] and was followed by further experimental tests of low-frequency behavior [*Chandler*, 1981; *Chandler and Johnson*, 1981], and of the influence of the porous frame modulus and tortuosity [*Johnson and Plona*, 1982; *Johnson et al.*, 1982]. Subsequent studies showed the slow wave could exist and propagate in a wide range of air- or water-saturated porous materials including bone [*Lakes et al.*, 1983], sintered metallic filters [*Jungman et al.*, 1989], aluminum foams [*Ji et al.*, 1998], textiles [*Gomez Alvarez-Arenas et al.*, 1994], soils [*Nakagawa et al.*, 1997], xerographic developer mixtures [*Stearns*, 1992] and anisotropic composites [*Castagnede et al.*, 1998]. Despite early conjectures that it could not exist in rock [*Klimentos and McCann*, 1988], the P2 mode has also been observed in real sandstones under air-saturated [*Nagy et al.*, 1990; *Nagy*, 1993; *Nagy et al.*, 1995] and water-saturated [*Kelder and Smeulders*, 1997; *Smeulders*, 2005] conditions. However, the high porosity and open pore networks afforded to experimentalists with sintered glass beads make this material popular in studies of the P2 wave [*Rasolofosaon*, 1988; *Wu et al.*, 1990; *Kurashige et al.*, 1992; *Johnson et al.*, 1994; *Geerits and Kelder*, 1997; *Gurevich et al.*, 1999; *Kurashige et al.*, 1999; *Zhu et al.*, 1999; *Derible*, 2004, 2005].

[6] To be clear at the outset, this contribution focuses on the observation and analysis of ultrasonic wave propagation in a highly permeable and porous material within the high-frequency regime of Biot theory, a regime in which both the P1 and P2 modes propagate as waves. This behavior differs from that of many real rocks in which crack-like porosity further complicates the problem with wave induced local flow mechanisms [e.g., *O'Connell and Budiansky*, 1974; *Mavko and Nur*, 1975; *Klimentos and McCann*, 1988; *Dvorkin et al.*, 1995; *Diallo and Appel*, 2000]; and this related and important issue is not relevant to this study on a highly porous, sintered glass-bead media.

## 3. Theoretical Considerations

### 3.1. Wave Modes in Saturated Porous Media

[7] The theoretical literature describing poroelastic wave propagation in fluid-saturated porous solids is large and need not be rehearsed in detail here. Both extensive [e.g., *Johnson*, 1984; *Bourbié et al.*, 1987; *Stoll*, 1989; *Allard*, 1993] and concise [e.g., *Haire and Langton*, 1999; *Smeulders*, 2005] descriptions may be found.

[8] Essentially, the theory considers an isotropic porous frame of porosity $\beta$ and permeability $K$ constructed of mineral grains of density $\rho_s$ and solid bulk modulus $K_s$ that are organized into a structure with a dry (or drained) frame bulk modulus $K_d$ and frame shear modulus $\mu_d$. The frame's pore network will also be characterized by the tortuosity $\xi = L/L_0$, where $L$ and $L_o$ are the tortuous and the straight path lengths, respectively. The fluid filling the connected pore space has shear viscosity $\eta$, mass density $\rho_f$, and bulk modulus $K_f$. The most intriguing result is that this saturated frame can support two longitudinal wave modes which are usually called the fast P1 and slow P2 modes that approximately correspond to the cases in which the fluid and solid portions are nearly in or out of phase, respectfully, with one another. The P2 mode is often also called the Biot slow wave. A third mode, the familiar shear wave S, also exists.

[9] It is worth reiterating that, broadly, the wave phenomenon may be separated into low- and high-frequency regimes. Viscous effects dominate at the low frequencies with the result that the motion of the fluid and solid components of the P1 mode are locked with its speed equal to that in *Gassmann*'s [1951] [*Johnson*, 1984] relations while the propagation of the P2 mode is better described by a diffusion equation than by a wave equation. In contrast, inertial effects are important in high-frequency regimes; the motions of the fluid and the solid are not as tied to one another and in such cases wave equations govern both P1 and P2 mode propagation. The relative size of the viscous skin depth $d = \sqrt{2\eta/\omega\rho_f}$ to the typical pore radius $r_o$ is generally assumed to control the boundary between low- and high-frequency behavior. Low-frequency viscous coupling occurs for $d > r_o$, while high-frequency inertial effects conduct when $d < r_o$. This study is well within the high-frequency regime with all three modes propagating; low-frequency effects will hereafter be ignored.

[10] For the sake of brevity, the final expressions are reported in terms of their angular frequency $\omega$ dependent and complex wave numbers $k_l$ in order to emphasize that both velocity and attenuation are important in this study. The dispersive phase velocities ($V_{P1}$, $V_{P2}$, and $V_S$) and the attenuation coefficients ($\alpha_{P1}$, $\alpha_{P2}$, and $\alpha_S$) may be obtained from the real and imaginary parts via $k_l(\omega) = (\omega/V_l) + i\alpha_l f$ assuming a linear attenuation model in the bandwidth of the wavefield generated by a source in a laboratory experiment.

**Table 1.** Required Physical Properties of Fluid, Solid, and Porous Frame

| Symbol | Name | Value | Units | Comment |
|---|---|---|---|---|
| $K_f$ | Fluid bulk modulus (water) | 2.209 (1%) | GPa | $\rho_f V_w^2$ |
| $K_s$ | Mineral bulk modulus | 43.7 (5%) | GPa | *Bass* [1995] |
| $V_{Pd}$ | Dry compressional wave speed | 2450 (2%) | m s$^{-1}$ | Measured by pulse transmission at 780 kHz |
| $V_{Sd}$ | Dry shear wave speed | 1555 (2%) | m s$^{-1}$ | |
| $V_w$ | Water wave speed | 1490 (0.5%) | m s$^{-1}$ | |
| $\alpha_P$ | Dry compressional wave attenuation | 6 (10%) | m$^{-1}$ | |
| $\alpha_S$ | Dry shear wave attenuation | 27 (10%) | m$^{-1}$ | |
| $K_d$ | Frame (drained, dry) bulk modulus | 4.826 | GPa | $\rho_D V_{Pd}^2 - 4\mu_d/3$ |
| $K_{un}$ | Frame unjacketed bulk modulus | 43.7 (5%) | GPa | Assumed = $K_s$ |
| $\mu_d$ | Frame shear modulus | 3.614 | GPa | $\rho_D V_{Sd}^2$ |
| $\beta$ | Porosity | 0.391 (2%) | dimensionless | Direct measure |
| $\xi$ | Tortuosity | 1.44 (10%) | dimensionless | Indirect measure from electrical conductivity[a] |
| K | Permeability | 19.9 (3.5%) | m$^{-2}$ × 10$^{-12}$ | Direct measure |
| $r_o$ | Pore radius (average) | 23 (20%) | $\mu$m | Hg porosimetry |
| $\gamma$ | Coefficient of fluid content | 0.202 | GPa$^{-1}$ | Equation (4) × 1.2 (see text) |
| $\eta$ | Dynamic shear viscosity | 0.001 | Pa s | *Watson et al.* [1980] |
| $\rho_s$ | Solid density | 2445 (1.5%) | kg m$^{-3}$ | Direct measure |
| $\rho_f$ | Fluid density | 995 (0.5%) | kg m$^{-3}$ | Direct measure |
| $\rho_B$ | Saturated bulk density | 1878 | kg m$^{-3}$ | $\beta\rho_f + (1-\beta)\rho_s$ |
| $\rho_D$ | Dry bulk density | 1489 | kg m$^{-3}$ | $(1-\beta)\rho_s$ |
| $\rho_{12}$ | Induced inertial mass | −170.8 | kg m$^{-3}$ | Equation (2) |

[a]Calculated from measured electrical conductivities (see *Bouzidi* [2003] for procedure).

The complex wave numbers for the two longitudinal wave modes are given by

$$k_l = \omega\left[\frac{\varsigma_l(1-\beta)\rho_s + \beta\rho_f}{\varsigma_l(A+2\mu_d) + R + Q}\right]^{1/2} \tag{1a}$$

where the subscript $l$ = P1 or P2 denotes either of the longitudinal modes, A, R, and Q are the Biot parameters [*Biot and Willis*, 1957; *Green and Wang*, 1986; *Kumpel*, 1991; *Hickey et al.*, 1995] but modified here, and $\zeta_l$ is a frequency-dependent parameter that primarily connects the solid and the fluid components (see Appendix A for derivation); these parameters are all defined in Appendix A and Table 1. The complex wave number for the single transverse shear wave S is similarly

$$k_3 = \omega\left[\frac{\varsigma_3(1-\beta)\rho_s + \beta\rho_f}{\varsigma_3\mu_d}\right]^{1/2} \tag{1b}$$

where again $\zeta_3$ describes the fluid-solid relationship.

[11] The different particle motions of the fluid against the solid that are possible require the $\zeta$ terms that account for both viscous and inertial drag effects. The former is important to attenuation and here the tilted Poisseuille flow assumption given by *Johnson et al.* [1987] is used. Too, the latter requires the introduction of an induced mass $\rho_{12}$ (see Appendix A). Using the physical properties of the sample given in Table 1, the velocities and attenuations are calculated from equations (1a) and (1b) and given in Table 2.

### 3.2. Modeling of Reflection and Transmission

[12] A full description of porous media behavior cannot be understood without knowledge of wave reflection, conversion, and transmission effects at the interface of a porous medium. In a practical sense, such knowledge is necessary to properly interpret laboratory observations [*Dutta*, 1980; *Wu et al.*, 1990; *Santos et al.*, 1992; *Johnson et al.*, 1994; *Aknine et al.*, 1997; *Gurevich et al.*, 1999; *Derible*, 2005] particularly if amplitudes and attenuation are considered. The problem is also of obvious consequence to seismic and sonar studies [e.g., *Stoll and Kan*, 1981; *Krebes*, 1984; *Delacruz et al.*, 1992; *Yang and Sato*, 1998; *Yang*, 1999; *Denneman et al.*, 2002; *Carcione and Helle*, 2004; *Tajuddin and Hussaini*, 2005] as the field observations of the variations of seismic amplitudes with angle of incidence become an increasingly important geophysical tool.

[13] The solution to this problem is, relative to that for a fluid (with only the compressional P wave allowed) over an isotropic elastic solid (with only P1 and S allowed), complicated by the fact that it is highly sensitive to the boundary conditions employed [e.g., *Deresiewicz and Skalak*, 1963; *Rasolofosaon*, 1988; *Gurevich and Schoenberg*, 1999], by the existence of three distinct waves, and because

**Table 2.** Comparison of Calculated and Observed Wave Velocities and Attenuations at 780 kHz

| | | | | Calculated | | Observed | |
|---|---|---|---|---|---|---|---|
| Symbol | Name | Units | PMMA | Low Frequency[a] | High Frequency | Saturated | Dry |
| $V_{P1}$ | Fast P1 wave speed | m s$^{-1}$ | 2675 ± 30 | 2667 | 2700 | 2700 ± 55 | 2540 ± 50 |
| $V_S$ | S wave speed | m s$^{-1}$ | 1390 ± 10 | 1389 | 1500 | 1500 ± 50 | 1555 ± 30 |
| $V_{P2}$ | Slow P2 wave speed | m s$^{-1}$ | - | - | 1030 | 1010 ± 20 | - |
| $\alpha_{P1}$ | P1 attenuation | m$^{-1}$ | 9.4 ± 0.9 | - | 6 | 7 ± 1 | 6 ± 1 |
| $\alpha_S$ | S attenuation | m$^{-1}$ | 26.5 ± 2.7 | - | 36 | 44 ± 2 | 27 ± 3 |
| $\alpha_{P2}$ | P2 attenuation | m$^{-1}$ | NA | - | 75 | 69 ± 4 | - |

[a]Calculated using *Gassmann*'s [1951] relations.

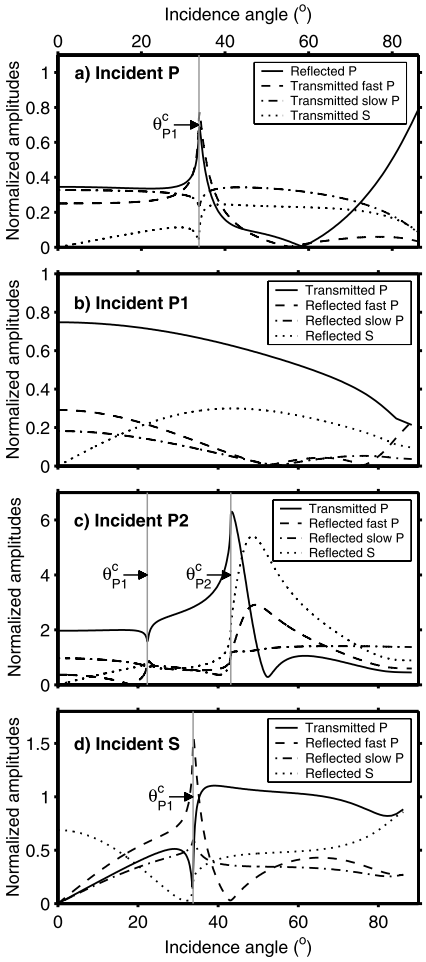


**Figure 1.** Modeled Plane wave reflected or transmitted amplitudes versus the angle of incidence at 780 kHz for the water saturated porous medium described in Table 1 for (a) P wave in water incident on the porous medium. (b) P1 (fast) wave in the porous medium incident on water. (c) P2 (slow) wave in the porous medium incident on water. (d) S wave in the porous medium incident on water. In Figures 1a–1d, the incident wave has an amplitude of unity for the average amplitude between the solid and the fluid components according to equation (2). Consequently, the transmitted P wave is larger than unity.

of the frequency dispersion of both wave speeds and attenuation. To carry out the modeling described below the solution for the transmitted conversions P-P1, P-S, and P-P2 as well as P1-P, P2-P, and S-P must be available, and the mathematics describing this problem as developed by *Deresiewicz and Skalak* [1963] is relegated to Appendix A.

[14] An example set of such plane wave reflection and transmission coefficients are shown in Figures 1a–1d for the four possible cases. The transmitted P in Figures 1b–1d is what is actually detected by the receiver. These are calculated at the peak frequency of the transducer which is ~780 kHz versus the angle of incidence. It should be noted that these coefficients are frequency-dependent. The calculations employ the actual measured physical properties given in Table 1 that are discussed in section 4. There are some aspects of the coefficients that are worth pointing out as they will be relevant to the later data.

[15] In each case, four reflected and transmitted modes are generated. Figure 1a shows the coefficients for the water-borne incident P wave onto the saturated porous medium. Defining the amplitude in a medium consisting of two independent phases must be done carefully, and it is important to mention that all reflection-transmission coefficients displayed in Figures 1a–1d are given for the average amplitudes in the fluid and the solid within the porous medium following the average procedure used by *Deresiewicz and Skalak* [1963]. For each wave mode in the porous medium the average amplitude is given by

$$A_{aver} = [\beta + (1-\beta)\zeta_l]A^f \tag{2}$$

where $A^f$ is the amplitude in the fluid which is related to that in the solid via $\zeta_1$.

[16] In Figure 1a, only the P-P1 critical angle $\theta^c_{P1} = 33.8°$ exists; as expected the transmitted P1 amplitudes rapidly decay past this point with a step increase in the transmitted S wave. The transmitted P2 mode is strong at all angles of incidence.

[17] For the incident fast P wave from the porous water interface no critical angles exist as all scattered waves have speeds smaller than that of the incident wave (Figure 1b).

[18] The coefficients for the incident P2 mode (Figure 1c) are the most complex as three critical angles exist ($\theta^c_{P2-P1} = 22.3°$, $\theta^c_{P2-S} = 43.2°$, and $\theta^c_{P2-P} \approx \theta^c_{P2-S}$). The transmitted P amplitude declines rapidly past $\theta^c_{P2-P}$ which may make observation of the P2 mode problematic at higher angles of incidence, but such high angles cannot be observed with the current experimental configuration.

[19] The amplitude of the slow P2 is dominated by fluid motion. Consequently, the transmitted P wave is larger than unity as the incident slow P wave is normalized with respect to the average amplitude. Finally, when a shear wave within the saturated medium is incident on water (Figure 1d), there is also only one critical angle for the S to P1 reflection ($\theta^c_{S-P1} = 33.8°$), and this is close to $\theta^c_{P-P1}$ due to the similarity in the speeds of P and S. The S to P transmission is particularly strong past this critical angle. At vertical incidence here, there are strong P1 and P2 reflections with P1 amplitude decaying with increasing angle of incidence.

[20] Most analyses proceed using these plane wave solutions only. However, as noted by others [e.g., *Rasolofosaon*, 1988; *Wu et al.*, 1990], real transmitting and receiving transducers are subject to diffraction. As such, the analysis of observed waveforms is confused by beam dimensions and by counterintuitive nonspecular effects [e.g., see *Bouzidi and Schmitt*, 2008]. Despite the fact that the amplitudes along the beam axis are stable the novel transmitter-receiver pair employed here is not immune to these effects; and a more complete modeling of the experiment that incorporates the transducer geometry was required. Indeed, this modeling eliminated the risk of misinterpretation of the observed waveforms as will be mentioned again later. No further assumptions or corrections are required to properly interpret the observed wave forms.

[21] The numerical modeling for the pulse transmission is already described [*Bouzidi and Schmitt*, 2006] and only a brief overview is necessary. The procedure begins by

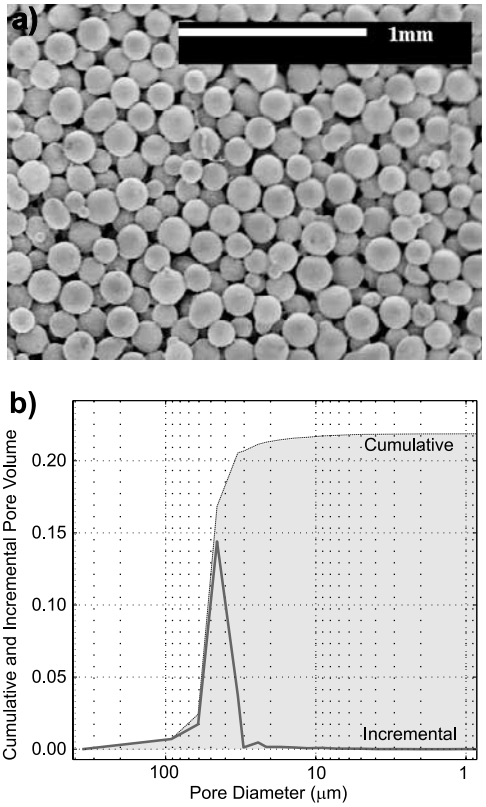


**Figure 2.** (a) Scanning electron micrograph image of sintered glass beads. (b) Cumulative (highlighted by filled region) and incremental (black line) volumes of Hg versus pore throat diameter as measured by Hg injection porosimetry.

propagating the experimentally obtained transmitter bounded pulse wavefield by Fourier domain phase-shifting methods that have been long employed in seismic modeling and migration algorithms [*Gazdag*, 1978]. Each wave number component is appropriately modulated at the interface by the complex reflection or transmission coefficients just mentioned. As such, each conversion and reflection must be individually considered; and the method should not be considered as a full wavefield modeling where the boundary conditions at interfaces would be implicitly accounted for. Consequently, individual modes can be modeled separately making event identification and interpretation simpler.

[22] The measurements from an acrylic (polymethyl methacrylate or PMMA) glass plate of the same dimensions are provided for purposes of comparison. This material serves as a foil to the porous media in that, while it is a nonporous solid with no possible P2 mode, its P1 and S wave speeds and attenuations are comparable (Table 2). The precursory study [*Bouzidi and Schmitt*, 2006] contains detailed information on its characterization and modeling.

## 4. Required Physical Properties of Sample

[23] The sample plate (22.0 cm × 22.0 cm × 2.46 cm) was manufactured by sintering glass beads by slowly increasing temperature to 700°C in a controlled glass shop oven for 4 h followed by a long cooling period to allow for slow stress release. This procedure follows a recipe similar to *Sen et al.* [1981]. The soda-lime glass beads are those typically used for sand blasting with diameters ranging predominantly between 150 and 212 $\mu$m, a SEM of a portion of the sample shows the details of the resulting structure (Figure 2a) while the results of Hg porosimetry (Figure 2b) provide an indication of the rather narrow distribution of pore throat diameters ($2r_o$) centered near 45.5 $\mu$m. The "grain" density $\rho_s$ of the glass beads and the porosity $\beta$ were determined by a standard water immersion technique (Table 1).

[24] Biot's formulation requires that a large number of parameters be determined (Table 1); the details of the measurements of these various parameters are given by *Bouzidi* [2003], and only a brief mention is given here. The distilled water density $\rho_f$ was directly measured using an Archimedean densitometer, the bulk modulus $K_f$ is inferred from a direct measurement of the wave speed in the fluid, while the water viscosity $\eta$ and the bulk modulus of the glass "mineral" grain $K_s$ are taken from literature. The Permeability $K$ was measured directly with water in a modified falling head permeameter. The tortuosity $\xi$ was determined from a specially designed electrical conductivity measurements [*Johnson et al.*, 1982] directly on the block that were then interpreted according to the theoretical assumptions of *Johnson et al.* [1982]. The frame bulk $K_{\mathrm{d}}$ and shear $\mu_d$ moduli were obtained from ultrasonic measurements of the compressional and shear wave speeds under open air "dry" conditions [e.g., *Johnson et al.*, 1987; *King et al.*, 2000]. It is important to note that the attenuation of these waves was also measured in independent experiments under dry conditions because, although the frame attenuation is not included in the standard poroelastic theory, this extra attenuation was necessary to reconcile the modeled and the observed experimental waveform as indicated in earlier work [*Wu et al.*, 1990]. The observed dry frame wave speeds and attenuations are provided in Table 2. A first-order frequency dependence is used to account for the losses in the dry frame. Within the frequency bandwidth source signal used in the experiments the losses are nearly linear. These losses in the dry frame can be explained by the fact that glass beads within the sample are not sintered completely. Therefore the glass beads have, to some extent, some compressional and rotational relative movement resulting in energy losses. The attenuation for the S wave is larger that for the P wave which can be explained by the fact that the beads have more freedom to rotate relative to each other than they have in the compressional mode.

[25] A number of additional parameters are not so directly obtained, these are the dynamic mass transfer $\rho_{12}$, the coefficient of fluid content $\gamma$, and the viscosity correction factor $F(\omega)$. These factors influence the final observed amplitudes; and they warrant some additional mention.

[26] One special aspect of poroelastic theory is that the negative inertial influence due to solid-fluid coupling must be considered. To complete the set of parameters given above that are needed for modeling wave propagation in fluid-saturated porous media the dynamic mass transfer $\rho_{12}$ and the viscosity correction factor, denoted $F(\omega)$ by *Biot* [1956b] must be determined. It is possible to infer $\rho_{12}$ from the measurement of the S wave velocity. However, $\rho_{12}$ is very sensitive to small variations of the S wave velocity.

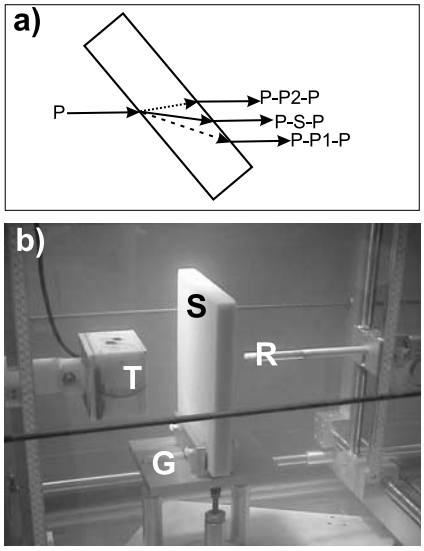


**Figure 3.** (a) Cartoon illustrating conversions and transmission of the water-borne P wave obliquely incident to the sample into the fast P1 (large dashes), the slow P2 (small dashes), and the shear S modes in the sample. (b) Photograph of experimental setup with large transmitting transducer T, small receiving transducer R, porous plate sample S, and goniometer G all submerged in water tank.

According to *Johnson et al.* [1987] this coefficient is independent of the mechanical properties of the solid and the fluid but it is always proportional to the fluid density and porosity. This coefficient is defined by

$$\rho_{12} = -(\xi - 1)\beta\rho_f \tag{3}$$

where $\xi$ is the tortuosity, $\beta$ is the porosity, and $\rho_f$ is the fluid density. As the two latter parameters are relatively well known, $\xi$ contributes the greatest uncertainty to $\rho_{12}$.

[27] The correction factor $F(\omega)$ involves complex processes involved in the fluid-solid interactions as a wave propagates through a porous medium. Workers have suggested a variety of pore configurations beginning with *Biot*'s [1956a, 1956b] initial model with Poiseuille flow through straight tubes. *Johnson et al.* [1987] employed a porous medium made of canted cylindrical tubes of radius $r_0$ (see Appendix A). $F(\omega)$ relies on knowledge of the $\rho_f$, $\eta$, and the pore throat radius $r_o$, a value of 23 $\mu$m in agreement with the average pore throat diameter of 45.5 $\mu$m given by Hg porosimetry was used in the calculations below.

[28] One final factor included in the theory is the coefficient of fluid content $\gamma$ that for a homogeneous and isotropic medium is [*Biot and Willis*, 1957; *Hickey and Sabatier*, 1997]

$$\gamma = \beta\left(\frac{1}{K_f} - \frac{1}{K_s}\right) \tag{4}$$

Equation (4) assumes that $K_{un} = K_s$. Many workers have commented that equation (4) may only apply under highly restrictive circumstances [see, e.g., *Hickey and Sabatier*, 1997]. In the later modeling it was found that a value 20% greater than that predicted by equation (4) yielded the best matches with the data. However, other factors might be in play for this discrepancy. For example, the porosity and the stiffness might not be uniform at the surfaces relative to the center of the sample. The stiffness might be slightly higher near the surfaces relative to the center of the sample.

## 5. Experimental Configuration

[29] The experimental configuration, including a detailed characterization of the specially constructed transducers employed, is already provided [*Bouzidi and Schmitt*, 2006] and only a brief overview is necessary here. The configuration (Figure 3) is similar to many other porous transmission studies that follow *Plona* [1980], but with the important difference that the current study employs a large transmitter and a near-point receiver combination. This arrangement simplifies the analyses in that the small receiver (1.9 mm $\times$ 1.9 mm) essentially senses the transmitted wave pressures at a point eliminating consideration of transducer aperture effects. The large transmitter was constructed using a sheet of piezoelectric ceramic (10.16 cm $\times$ 7.62 cm) to ostensibly provide a near-planar wavefront within the dimensions of the experiment. This ideal situation was not achieved completely, hence necessitating the wavefield modeling, but one unexpected benefit was a significant improvement in the transmitted signal quality abetted by a combination of lower beam spreading, directivity and increased pulse energy.

[30] During a series of measurements, the sample is placed vertically on the rotating table goniometer and between the immobile transmitter-receiver pair. The transmitter was activated using a $\sim$200 V step producing an acoustic pulse in the water that propagated through the sample to the receiver. The receiver voltage was recorded at a rate of 5 ns per sample using a digital oscilloscope (Tektronix TDS 420A) to obtain the observed waveform. The sample was rotated in order to change the effective incidence angle of the pulse; a waveform was acquired every 1° over the range of $-50°$ to $+50°$. The direct waveforms from the transmitter to the receiver were also obtained with the sample removed both before and after the sample measurements in order to monitor pulse consistency and to obtain the wave speed of the water in the experiment tank.

## 6. Results and Discussion

### 6.1. Character of Observed Waveforms and Wave Speeds

[31] The set of waveforms obtained in the nonporous viscoelastic acrylic (Figure 4a) [*Bouzidi and Schmitt*, 2006] are compared to those for the saturated sample (Figures 4b and 4c) (see the auxiliary material).[1] There are a number of features worth pointing out beginning with the PMMA plate which clearly shows the direct P1 and S refracted waves with wave speeds of 2665 and 1390 m s$^{-1}$, respectively. The low uncertainties are a consequence of being able to make numerous transit time measurements with both the direct refractions and the multiple reflections. Note that the

[1] Auxiliary material data sets are available at ftp://ftp.agu.org/apend/jb/2008jb006018. Other auxiliary material files are in the HTML.

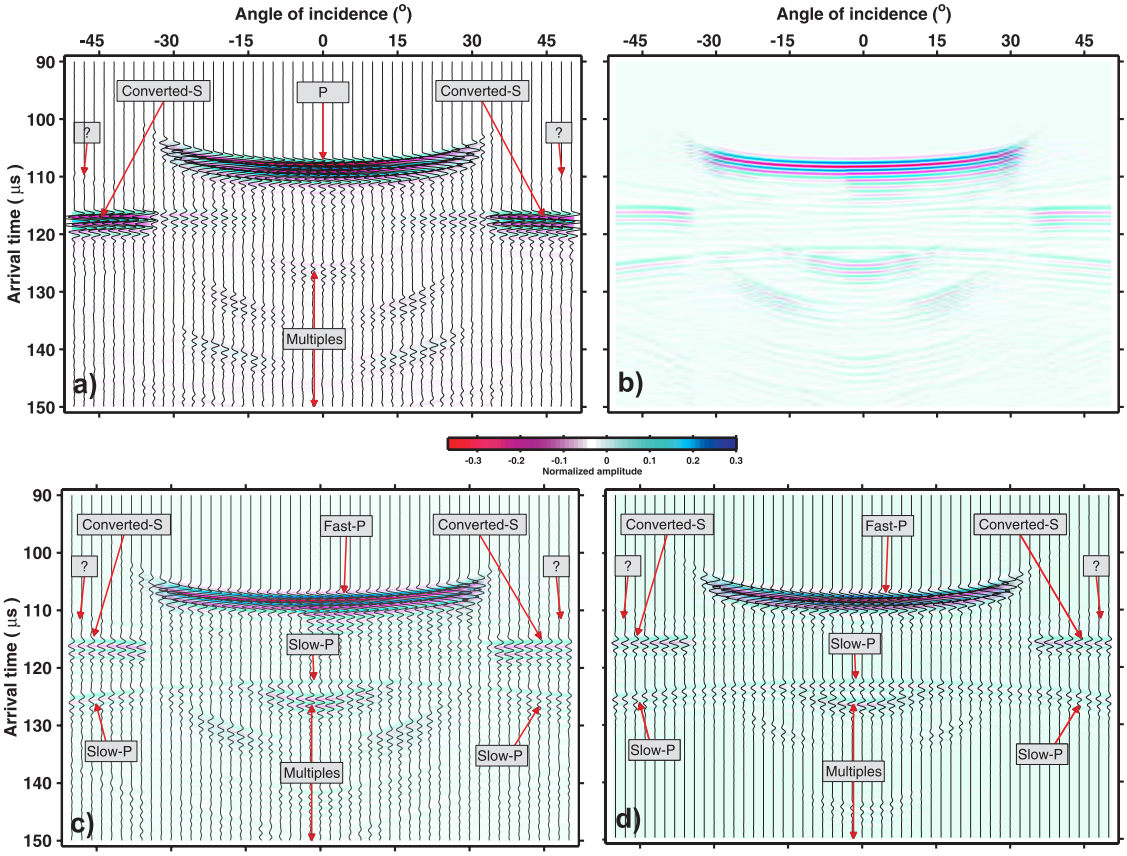


**Figure 4.** (a) Interpreted observed transmitted waveforms in normalized variable area for the nonporous acrylic PMMA plate shown for purposes of comparison. (b) Uninterpreted observed transmitted and unnormalized waveforms in false color amplitude image for the saturated porous plate. (c) Same as Figure 4b but with event interpretations applied. (d) Porous plate waveforms modeled using phase advance method.

P1 arrivals disappear at angles greater than its critical angle and that past this angle the strength of the transmitted S wave increases substantially as suggested by of the modeling of Figure 1. The P1 and S travel times versus angle of incidence curves agree with the P1 and S wave velocities measured independently on the PMMA plate by a standard contact pulse transmission measurement.

[32] An important point here is that there is a third arrival denoted by a question mark that could easily have been misinterpreted as a bulk mode through the sample. However, earlier transducer modeling [*Bouzidi and Schmitt*, 2006] demonstrated this to be only an artifact of the experimental geometry related to transducer edge effects. This further shows the utility of the large transmitter in that if smaller transducers are used this edge effect would be buried with the main arrival itself and could adversely influence measurements of attenuation. The event is clearly separated from the true direct body wave modes through use of this large transmitter. A number of multiple reverberations may also be detected. These can be interpreted on the basis of knowledge of P1 and S velocities for the PMMA using straightforward Snell's law arguments.

[33] The waveforms for the porous plate are similar to those for the PMMA but also include the additional P2 mode (Figures 4b and 4c). In contrast to S which, as expected, is weak or nonexistent near $\theta = 0°$, the P2 mode exists at all angles of incidence covered as expected (Figure 1). It must be noted that the input waveform character changed between the time those traces acquired at negative and those at positive incidence angles were acquired. In later quantitative analyses here, only positive incidence traces were fully reliable as the input waveform character was known well for these. Consequently, the negative waveforms were normalized with respect to the positive waveforms using the first arrival amplitudes.

[34] An independent measurement of these saturated wave speeds does not exist and the wave speeds (Table 2) are obtained by analysis of the travel time curves of Figure 4b. The numerous waveforms available together with the fact that the travel path lengths also vary with angle of incidence allow the frequency-dependent phase velocities and attenuations to also be determined using Fourier domain methods [e.g., *Molyneux and Schmitt*, 2000]. The plots of wave speeds versus frequency for each of the three modes (Figure 5) exhibit little evidence for dispersion across the relatively narrow frequency band of [0.5–1. MHz]. These wave speeds were further checked by using them to calculate the expected arrival times as a function of the angle of incidence, these times agreed with those from the observed waveforms of Figure 4b.

[35] The calculated wave speeds (Table 1) agree well with those measured. It is noticed that the induced mass $\rho_{12}$

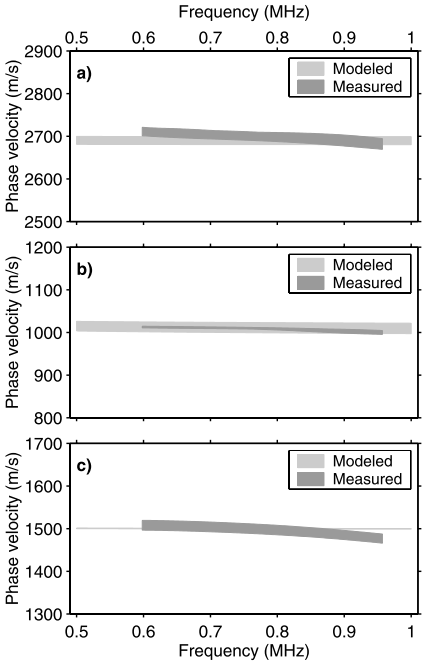


**Figure 5.** Comparison of calculated and observed phase velocities versus frequency for (a) the P1 wave, (b) the P2 wave, and (c) the S wave. Gray area represents zone of possible calculated solutions, while the dark area is the observed values including uncertainty.

influences the velocity of both the slow P wave and the S wave whereas the fast P wave is not sensitive to this parameter. The phase shift modeling resulted in a very good agreement with the observations both in amplitude and phase as the real amplitude displays shows (Figure 4d).

### 6.2. Attenuation

[36] The theoretical attenuation curves $\alpha(f)$ inclusive of any additional frame attenuation are calculated for the P1, P2, and S modes (Figure 6) using the parameters of Table 1 and the imaginary parts of equations (1a) and (1b). In order to obtain a simpler expression for comparison with the observed data, these theoretical curves are empirically fit by an exponential function. Following *Courtney and Mayer* [1993] a function of the form $a_o f^N$ where $a_o$ is the frequency-independent attenuation coefficient constant, $f$ is the frequency, and $N$ is an exponent that varies in general from 2 to 0.5 was used. Of course, this formula has no inherent physical basis but it does describe well the attenuation curves with values of 0.9 (i.e., nearly linear) for the P1 and S modes and 0.5 for the P2 mode (Figure 6).

[37] Determination of attenuation is always problematic. Initially, standard spectral ratio methods [e.g., *Molyneux and Schmitt*, 2000] were applied, but the results were not satisfactory due to this technique's sensitivity to noise and interference between the various modes and their multiples. A different approach was used where the attenuation of a given mode is estimated by a direct waveform analysis guided by the empirical exponential functions just described. Briefly, this analysis consists of the following:

[38] 1. First, modulate the observed waveforms, after they are normalized with respect to the known incident pulse, by their appropriate angle of incidence transmission coefficients at each boundary. Over the limited bandwidth [0.5–1.0 MHz] the change in the value of these coefficients was small for a given angle of incidence. The transmission coefficients at the peak frequency, calculated as a frequency-dependent coefficient was used. However, in the modeling procedure the transmission coefficients used are still frequency-dependent. This gives the amplitudes that would be expected in the case with no attenuation whatsoever.

[39] 2. This signal is then further modulated, but on this occasion within the frequency domain, by a trial value of $\alpha_o$ (as defined above) for the particular mode studied and using the appropriate mode-dependent exponent N as discussed above. This result is inverse transformed to the time domain to obtain a trial waveform.

[40] 3. The trial waveform is compared directly to that observed. We have found that comparison is facilitated by examining the absolute value of the analytic signals (i.e., the amplitude envelope).

[41] 4. This procedure is repeated until the best match between the calculated and the observed curves is reached; the "observed" attenuation is then calculated from the best value of $\alpha_o$.

[42] The results of this analysis are shown for attenuation versus frequency in Figures 7a–7c as the dark gray strip whose vertical width of which represents the uncertainty of the analysis method above (see uncertainties of input parameters in Table 1). Ideally, in the absence of the frame attenuation this dark gray strip would match the theoretical prediction of equations (1a) and (1b) shown as a dashed line

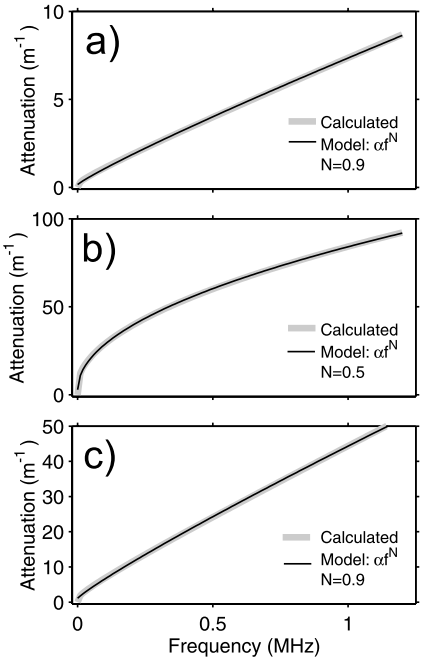


**Figure 6.** Calculated attenuation versus frequency for the case of a Biot porous medium and excluding frame attenuation (thick gray line) on the basis of the physical properties of Table 1 for the (a) P1, (b) P2, and (c) S waves. Corresponding empirical fits using the exponential expression and the best exponent N for each case are shown as a dark line.

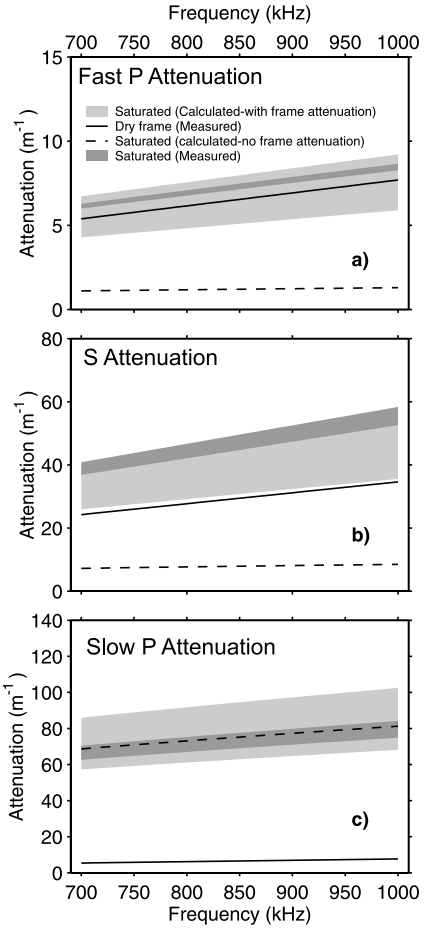


**Figure 7.** Comparison of the observed saturated (dark gray area), the dry frame (solid line) attenuations with those calculated assuming that the frame does (light gray region) and does not (dashed line) influence the overall attenuation of the Biot porous medium for (a) the P1 wave, (b) the S wave, and (c) the P2 wave.

in Figure 7. It is important to point out that the observed and the ideal predicted curves differ substantially for the P1 and S modes but are in good agreement for the P2 mode.

[43] To further examine this discrepancy, the observed attenuation for the dry frame is shown as a solid line in Figure 7. The dry frame attenuation has little influence on the P2 mode but that for the dry P1 wave already plotted in Figure 7a is repeated for comparative purposes. The dry attenuation of the P1 wave is much less than that for the S wave, the reason for this is not known but it may be associated with the weak bonding of the glass beads during the light sintering process.

[44] Only once the attenuation of the dry frame is included are the observed P1 and S attenuations in good agreement with those observed. The P1 and S mode attenuations are dominated by the frame's intrinsic dry attenuations. It is also worth noting that a linear model (N = 1) was used to describe the frame attenuation included in the theoretical calculations.

[45] The frame attenuation does not appear to significantly influence the observed attenuation of the P2 wave. Indeed,

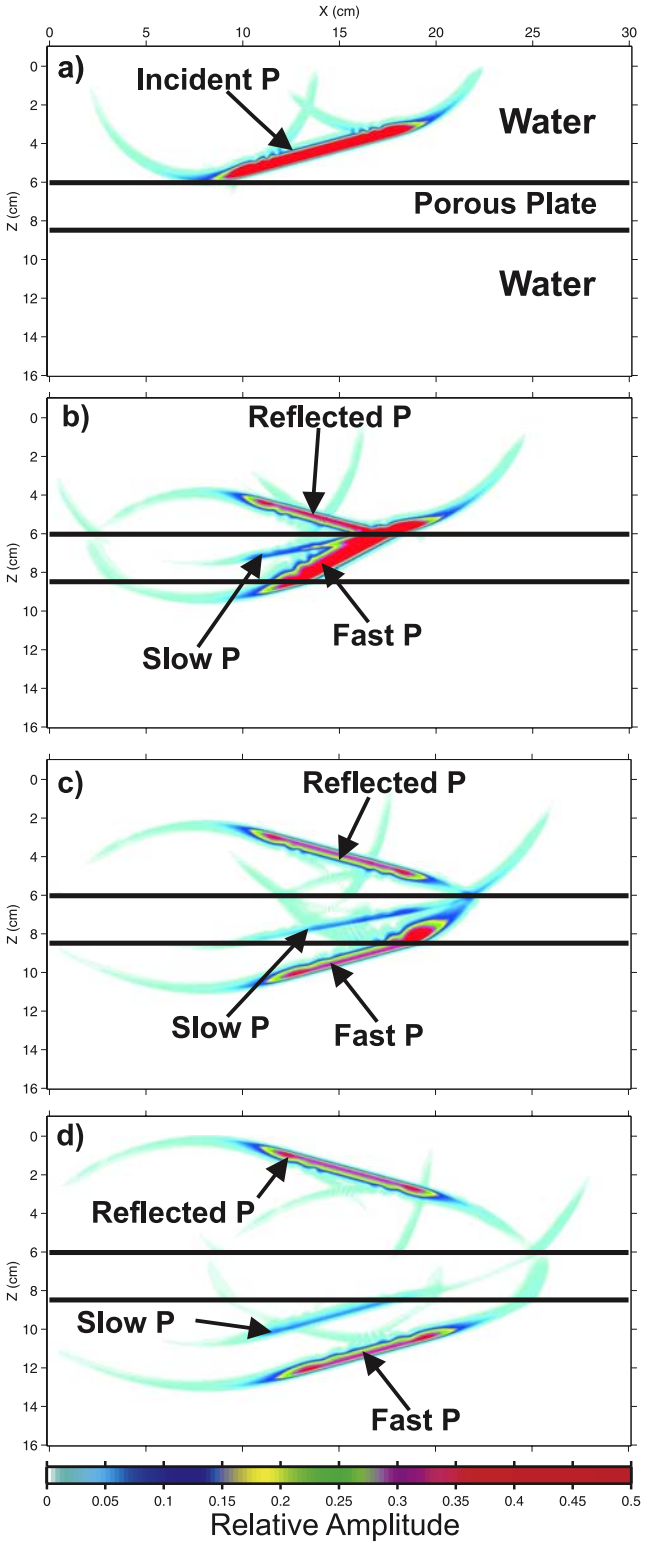


**Figure 8.** Fully modeled incident P, reflected P, transmitted fast P, and transmitted slow P as time snapshots at (a) 44 $\mu$s, (b) 60 $\mu$s, (c) 70 $\mu$s, and (d) 84 $\mu$s. Note that high amplitudes particularly those of the incident and transmitted fast waves are clipped in order to better visualize lower-amplitude events. (See Animation S1 in the auxiliary material.)

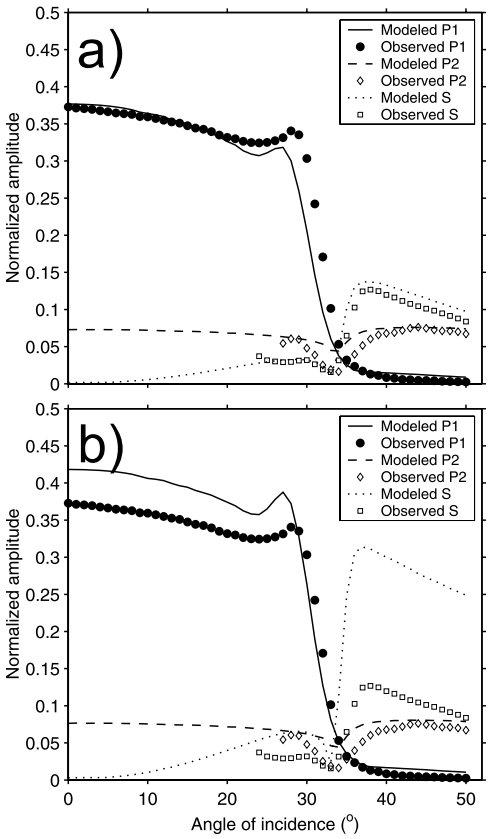


**Figure 9.** Comparison between fully modeled (lines) and observed (symbols) peak ultrasonic waveform amplitudes for cases that (a) include and (b) ignore the frame attenuation. Observed amplitudes for P1, P2, and S modes represented by black circles, open diamonds, and open squares, respectively. Corresponding calculated amplitudes for the P1, P2, and S modes are represented by continuous, dashed, and dotted lines, respectively.

the theoretically expected and the observed P2 attenuation match within the uncertainty without additional correction.

### 6.3. Modeling and Final Amplitudes

[46] As noted in section 6.1, Figure 4d shows the set of waveforms modeled using the phase advance technique and the physical values in Tables 1 and 2, these agree well with those observed in Figure 4b. The fully modeled reflected and transmitted fast and slow P waves are shown in Figure 8 as snapshots at 44, 60, 70, and 84 $\mu$s. The attenuation is noticeable for the slow P wave as the amplitude decays away from the first water-porous interface in Figures 8b and 8c. The theoretically expected and observed waves speed and attenuations are, too, in good agreement. One final and perhaps more sensitive test, however, is a direct comparison of the observed wave amplitudes with those fully modeled including transducer diffractions, transmission losses, and attenuations either excluding (Figure 9b) or including via the complex $\mu_d$ and $K_d$ (Figure 9a) the frame losses. The amplitudes reported (Figure 9) are those of the peak magnitude of the analytic signal (i.e., the peak value of the amplitude envelope or the magnitude of the analytic signal as described by *Bouzidi and Schmitt* [2006]). The observed results are shown as discrete symbols while those calculated appear as lines. When the frame attenuation is not considered the modeled amplitudes for the P1 and the S modes exceed those observed (Figure 9a), the discrepancy of the S wave is particularly large. Again, the differences are reduced once frame attenuation is included. The problem of frame attenuation had previously been mentioned as one possible reason for the lack of agreement between the expected and observed amplitudes of *Wu et al.* [1990] and *Rasolofosaon* [1988] although neither of these authors included the transmission and transducer diffraction effects in their analysis.

[47] The effects of the wave amplitudes [e.g., *Mavko*, 1979; *Johnston and Toksoz*, 1980; *Mashinskii*, 2006] have not been considered in this analysis. While this may play a role at higher wave intensities, the relatively good agreement between the observations and theory here suggest that amplitude-dependent mechanisms are not necessary at the current signal strengths.

## 7. Conclusions

[48] A novel ultrasonic goniometer system that employs a large transmitter was used in the acquisition of waveforms transmitted through a water-saturated porous sample at a range of angles of incidence. The Biot slow P2 wave was observed at all angles. The porous medium, consisting of sintered glass beads, was fully characterized allowing the saturated fast P1, the slow P2, and the shear S wave speeds and attenuations to be predicted to those extracted from the observed waveforms. Forward modeling of the waveforms incorporated the predicted waves speeds and attenuations, transducer effects, and wave transmissivity and conversion. The modeled waveforms agree well with those observed. Consequently, these tests lend further support existing poroelastic theory as begun by *Biot* [1956a, 1956b] and modified by later workers [*Johnson et al.*, 1982, 1987] in general. Most critically, the consistency between the final observed and modeled amplitudes for the three waves supports the use of open flow boundary conditions in such cases. A further important conclusion is that the attenuation of the porous frame does not measurably affect the transmission of the slow P2 wave.

[49] Three parameters are difficult to constrain because their definitions remain incomplete and are to a large degree developed using phenomenological arguments. These include the induced mass coefficient $\rho_{12}$, the coefficient of fluid content $\gamma$, and the frequency-dependent viscous correction factor $F(\omega)$. Best matching of the modeled to the observed waveforms required that the value of $\gamma$ be adjusted modestly relative to a direct application of the theory. Despite this, direct application of the theory gave results that differed from the observations by only a few percent.

[50] In summary, on one hand the Biot theory appears to adequately describe the wave propagation through and the transmissivity of the interfaces of a liquid filled porous medium, at least for such highly porous samples and at ultrasonic frequencies: a positive result. On the other hand, one might ask why such a theory should work at all given the rather simple phenomenological nature of the tube-like pores of *Biot* [1956b] and for that matter *Johnson et al.* [1987]. Such tubes are at best a crude description of real tortuous pore networks. It would be useful to continue these

studies on lower-porosity materials and in materials with more complex pore structures to see at which point the Biot descriptions will fail.

[51] Forthcoming work will examine the first surface ultrasonic reflectivity of this porous sample. The characterization of the sample described here is a necessary step toward this goal.

## Appendix A: Theory Detail

[52] This appendix provides a new approach in looking at the Biot theory. It will emphasize on the dynamic drag factors that link the solid and the fluid for each wave mode that can propagate in a fluid-saturated porous medium. Extensive explanation may is given by *Bouzidi* [2003, chapter 4 and appendices].

### A1. Longitudinal Wave Propagation

[53] The equation of motion for longitudinal waves in terms of potential fields $\phi^{(s)}$ and $\phi^{(f)}$ in the solid and fluid, respectively, are given by

$$\begin{aligned}(1-\beta)\rho_s\frac{\partial^2}{\partial t^2}\phi^{(s)} - \rho_{12}\frac{\partial^2}{\partial t^2}\left(\phi^{(s)}-\phi^{(f)}\right) + F(\omega)\frac{\eta\beta^2}{K}\frac{\partial}{\partial t}\\ \cdot\left(\phi^{(s)}-\phi^{(f)}\right)\\ = \nabla^2\left[(A+2\mu_d)\phi^{(s)} + Q\phi^{(f)}\right]\\ \beta\rho_f\frac{\partial^2}{\partial t^2}\phi^{(f)} + \rho_{12}\frac{\partial^2}{\partial t^2}\left(\phi^{(s)}-\phi^{(f)}\right) - F(\omega)\frac{\eta\beta^2}{K}\frac{\partial}{\partial t}\\ \cdot\left(\phi^{(s)}-\phi^{(f)}\right)\\ = \nabla^2\left[Q\phi^{(s)} + R\phi^{(f)}\right]\end{aligned} \tag{A1}$$

where the material properties required are described in Table 1 above. $A$, $Q$, and $R$ are the Biot parameters and $F(\omega)$ is a viscosity correction factor. Let the solid/fluid ratio be $\zeta_l = \phi^{(s)}/\phi^{(f)}$ where $l$ = 1,2 for the fast and slow waves, respectively, and let $\tilde{\rho}_{12} = \rho_{12} + iF(\omega)(\eta\beta^2/K\omega)$. For plane waves, equations (A1) lead to

$$\begin{aligned}\left[k_l^2(A+2\mu_d) - \omega^2((1-\beta)\rho_s - \tilde{\rho}_{12})\right]\phi^{(s)} + \left[k_l^2 Q - \omega^2\tilde{\rho}_{12}\right]\phi^{(f)} = 0\\ \left[k_l^2 Q - \omega^2\tilde{\rho}_{12}\right]\phi^{(s)} + \left[k_l^2 R + \tilde{\rho}_{12}\omega^2 - \omega^2\beta\rho_f\right]\phi^{(f)} = 0\end{aligned} \tag{A2}$$

Eliminating $k_l$ from (A2) we obtain a quadratic equation in $\zeta_l$

$$a\zeta^2 + b\zeta + c = 0 \tag{A3}$$

where $a$, $b$, and $c$ are given by

$$a = -(A+2\mu_d+Q)\tilde{\rho}_{12} + Q(1-\beta)\rho_s \tag{A4a}$$

$$b = (A+2\mu_d-R)\tilde{\rho}_{12} - (A+2\mu_d)\beta\rho_f + R(1-\beta)\rho_s \tag{A4b}$$

$$c = (Q+R)\tilde{\rho}_{12} - Q\beta\rho_f \tag{A4c}$$

which can easily solved for $\zeta_l$.

[54] The parameter $k_l$ can be easily derived from either equation (A4a) or (A4b). It can be also obtained in a compact form by adding equation (A1) which lead to

$$k_l = \omega\left[\frac{\varsigma_l(1-\beta)\rho_s + \beta\rho_f}{\varsigma_l(A+2\mu_d) + R + Q}\right]^{1/2} \tag{A5}$$

The combined solid-fluid coupling drag terms incorporate both inertial and viscous drag forces; $\zeta_1$ and $\zeta_2$ are determined from the two zeros of the quadratic formula (A3).

[55] The Biot parameters here are

$$\begin{aligned}A &= \frac{(K_s - K_s\beta - K_d)^2}{K_s + \gamma K_s^2 - K_d} + K_d - \frac{2}{3}\mu_d\\ Q &= \frac{\beta K_s(K_s - K_s\beta - K_d)}{K_s + \gamma K_s^2 - K_d}\\ R &= \frac{\beta^2 K_d^2}{K_s + \gamma K_s^2 - K_d}\end{aligned} \tag{A6}$$

and $\gamma$, the coefficient of fluid content, is given by

$$\gamma = \beta\left(\frac{1}{K_f} - \frac{1}{K_s}\right) \tag{A7}$$

The coefficient of fluid content assumes that $K_{un} = K_s$. If this is not true then this coefficient might be calculated as follows [*Hickey and Sabatier*, 1997]:

$$\gamma = \beta\left(\frac{1}{K_f} - \frac{1}{K_s}\right) + (1-\beta)\left(\frac{1}{K_{un}} - \frac{1}{K_s}\right) \tag{A8}$$

### A2. Rotational Wave Propagation

[56] Rotational wave propagation the Biot equations of motion in terms of potential fields $\vec{\psi}^{(s)}$ and $\vec{\psi}^{(f)}$ in the solid and fluid components, respectively, are given by

$$\begin{aligned}(1-\beta)\rho_s\frac{\partial^2}{\partial t^2}\vec{\psi}^{(s)} - \rho_{12}\frac{\partial^2}{\partial t^2}\left(\vec{\psi}^{(s)}-\vec{\psi}^{(f)}\right)\\ + F(\omega)\frac{\eta\beta^2}{K}\frac{\partial}{\partial t}\left(\vec{\psi}^{(s)}-\vec{\psi}^{(f)}\right) = \mu_d\nabla^2\vec{\psi}^{(s)}\\ \beta\rho_f\frac{\partial^2}{\partial t^2}\vec{\psi}^{(f)} + \rho_{12}\frac{\partial^2}{\partial t^2}\left(\vec{\psi}^{(s)}-\vec{\psi}^{(f)}\right)\\ - F(\omega)\frac{\eta\beta^2}{K}\frac{\partial}{\partial t}\left(\vec{\psi}^{(s)}-\vec{\psi}^{(f)}\right) = 0\end{aligned} \tag{A9}$$

For plane wave solutions and using $\tilde{\rho}_{12}$ as defined above (A9) lead to

$$\left[k_3^2\mu_d - \omega^2((1-\beta)\rho_s + \tilde{\rho}_{12})\right]\vec{\psi}^{(s)} - \omega^2\tilde{\rho}_{12}\vec{\psi}^{(f)} = 0 \tag{A10a}$$

$$\tilde{\rho}_{12}\vec{\psi}^{(s)} + \left[\beta\rho_f - \tilde{\rho}_{12}\right]\vec{\psi}^{(f)} = 0 \tag{A10b}$$

Equation (A10a) gives the solid-fluid ratio

$$\zeta_3 = -\frac{\beta\rho_f - \tilde{\rho}_{12}}{\tilde{\rho}_{12}} \tag{A11}$$

Equations (A9) can be combined to obtain the shear wave number

$$k_3 = \omega\left[\frac{\varsigma_3(1-\beta)\rho_s + \beta\rho_f}{\varsigma_3\mu_d}\right]^{1/2} \tag{A12}$$

The viscosity correction factor as given by *Johnson et al.*'s [1987] canted tube formulation

$$F(\omega) = \frac{-2ixJ_1\left[4(ix)^{1/2}\right]}{2(ix)^{1/2}J_0\left[4(ix)^{1/2} - J_0\left(4(ix)^{1/2}\right]\right.} \tag{A13}$$

where $x = r_0^2\rho_f\omega/16\eta$ and $J_0$ and $J_1$ are Bessel functions was used in the calculations. It is important to note that equation (A13) does not depend on the tortuosity nor on the slanting angle [*Johnson et al.*, 1987] when defined as $\xi = 1/\cos\ \alpha^2$. The measured tortuosity by pure electrical conductivity experiment would lead to an angle $\alpha = 33.6°$ for the slanted tube model given in (A13).

### A3. Plane Wave Solution Reflection and Transmission Coefficients

[57] The reflection and transmission boundary value problem between a fluid and a fluid-saturated porous material is solved using the *Deresiewicz and Skalak* [1963] boundary conditions that are (1) the normal total stress on the bulk material of the porous medium and the stress in the fluid medium must be continuous at the boundary, (2) the tangential stress in the porous medium must vanish at the boundary, (3) the fluid pressure must be continuous across the boundary, and (4) the normal component of the averaged particle velocity over the bulk material in medium $b$ and the normal fluid particle velocity in medium $a$ must be continuous at the boundary. which may be mathematically represented as

$$\begin{aligned}
&\{\sigma_{zz} + s\}_b = \left\{-p^{(f)}\right\}_a \\
&\{\sigma_{xz}\}_b = 0 \\
&\left\{-p^{(f)}\right\}_b = \left\{-p^{(f)}\right\}_a \\
&\left\{(1-\beta)v_z^{(s)} + \beta v_z^{(f)}\right\}_b = \left\{v^{(f)}\right\}_a
\end{aligned} \tag{A14}$$

where $\sigma_{zz}$ is the normal stress, $\sigma_{xz}$ is the tangential stress, $s$ is the stress in the fluid, $p^{(f)}$ is the pressure, $\nu_z$ is the vertical component of the particle velocity, and $\nu$ is the fluid velocity. For the first case shown in Figure 1a of a P wave in water incident on the saturated medium four waves are generated at the boundary: a reflected P wave, and transmitted fast P1, slow P2, and S waves. Let the superscripts $(f)$ and $(s)$ represent the potentials and coefficients for the fluid and the solid portions, respectively, and the subscripts 1, 2, and 3 for the P1, P2, and S modes, respectively. The potentials are for

Incident P

$$\phi_{inc}^{(f)} = e^{i(\omega t - k_x x - k_z z)} \tag{A15a}$$

Reflected P

$$\phi_{ref} = Ee^{i(\omega t - k_x x + k_z z)} \tag{A15b}$$

Transmitted P1

$$\phi_1^{(f)} = B^{(f)}e^{i(\omega t - k_{1x}x - k_{1z}z)}, \phi_1^{(s)} = \zeta_1 B^{(f)}e^{i(\omega t - k_{1x}x - k_{1z}z)} \tag{A15c}$$

Transmitted P2

$$\phi_2^{(f)} = C^{(f)}e^{i(\omega t - k_{2x}x - k_{2z}z)}, \phi_2^{(s)} = \zeta_2 C^{(f)}e^{i(\omega t - k_{2x}x - k_{2z}z)} \tag{A15d}$$

Transmitted S

$$\vec{\psi}_1^{(f)} = D^{(f)}e^{i(\omega t - k_{3x}x - k_{3z}z)}, \vec{\psi}_1^{(s)} = \zeta_1 D^{(f)}e^{i(\omega t - k_{3x}x - k_{3z}z)} \tag{A15e}$$

where $E$, $B^{(f)}$, $C^{(f)}$, and $D^{(f)}$are the respective reflection or transmission coefficients to be determined and plotted in Figure 1. These may be written as a vector $\mathbf{X} = [B^{(f)}\ C^{(f)}\ D^{(f)}\ E]$. Application of the boundary conditions to the potentials eventually results in a solution that may be distilled to a matrix form

$$\mathbf{TX} = \mathbf{G} \tag{A16}$$

where $\mathbf{T}$ is a $4 \times 4$ matrix of known physical parameters

$$\mathrm{T} = \begin{bmatrix}
2\mu_M\zeta_1 k_{1z}^2 + (A\zeta_1 + Q)k_1^2 + k_1^2(Q\zeta_1 + R) & 2\zeta_1 k_{1x}k_{1z} & \dfrac{k_1^2(Q\zeta_1 + R)}{\beta} & [(1-\beta)\zeta_1 + \beta]k_{1z} \\
2\mu_M\zeta_2 k_{2z}^2 + (A\zeta_2 + Q)k_2^2 + k_2^2(Q\zeta_2 + R) & 2\zeta_2 k_{2x}k_{2z} & \dfrac{k_2^2(Q\zeta_2 + R)}{\beta} & [(1-\beta)\zeta_2 + \beta]k_{2z} \\
2\mu_M\zeta_3 k_{3x}k_{3z} & \zeta_3\left(k_{3x}^2 - k_{3z}^2\right) & 0 & [(1-\beta)\zeta_3 + \beta]k_{3x} \\
-\rho_f\omega^2 & 0 & -\rho_f\omega^2 & k_z
\end{bmatrix} \tag{A17}$$

$\mathbf{G}$ is also a known vector that depends on the incident wave considered and is explicitly for the case of P incident onto a saturated medium:

$$\mathbf{G} = \left[\rho_f\omega^2\ 0\ \rho_f\omega^2\ k_z\right] \tag{A18a}$$

For the other three cases with P1, P2, and S waves within the porous medium being reflected and with only the P

wave in the liquid being transmitted $\mathbf{X} = [B^{(f)}\ C^{(f)}\ D^{(f)}\ E]$ and G becomes

Case with incident P1

$$G = \begin{bmatrix} -2\mu_M \zeta_1 k_{1z}^2 - (A\zeta_1 + Q)k_1^2 + k_1^2(Q\zeta_1 + R) \\ -2\zeta_1 k_{1x} k_{1z} \\ -\dfrac{k_1^2(Q\zeta_1 + R)}{\beta} \\ -[(1-\beta)\zeta_1 + \beta]k_{1z} \end{bmatrix} \quad \text{(A18b)}$$

Case with incident P2

$$G = \begin{bmatrix} -2\mu_M \zeta_2 k_{2z}^2 - (A\zeta_2 + Q)k_2^2 + k_2^2(Q\zeta_2 + R) \\ -2\zeta_2 k_{2x} k_{2z} \\ -\dfrac{k_2^2(Q\zeta_2 + R)}{\beta} \\ -[(1-\beta)\zeta_2 + \beta]k_{2z} \end{bmatrix} \quad \text{(A18c)}$$

Final case of incident S

$$G = \begin{bmatrix} -2\mu_M \zeta_3 k_{3x} k_{3z} \\ -2\zeta_2 k_{2x} k_{2z} \\ 0 \\ -[(1-\beta)\zeta_3 + \beta]k_{3x} \end{bmatrix} \quad \text{(A18d)}$$

[58] **Acknowledgments.** This work was supported through NSERC Discovery and Equipment Grants, and the Canada Research Chairs program to D.R.S. The assistance of G. Lachat, T. Paget, L. Tober, and P. Zimmerman in the development of the experimental apparatus was crucial. Discussions and insight from J. Beamish, V. de la Cruz, C. Hickey, E. Krebes, R. J. O'Connell, and T. J. Spanos were invaluable. The suggestions of two reviewers were also greatly appreciated.

## References

Aknine, A., B. Castagnede, and C. Depollier (1997), Reflection/refraction of acoustic waves on an interface fluid/porous material, *C. R. Acad. Sci., Ser. B*, *324*, 501–511.

Allard, J.-F. (1993), *Propagation of Sound in Porous Media: Modelling Sound Absorbing Materials*, 284 pp., Elsevier Sci., London.

Allard, J. F., C. Depollier, and A. Lesperance (1986), Observation of the Biot slow-wave in a plastic foam of high flow resistance at acoustical frequencies, *J. Appl. Phys.*, *59*, 3367–3370, doi:10.1063/1.336801.

Bass, J. D. (1995), Elasticity of minerals, glasses, and melts, in *Mineral Physics and Crystallography: A Handbook of Physical Constants*, edited by T. J. Ahrens, *AGU Ref. Shelf*, *2*, 45–63, AGU, Washington, D. C.

Beamish, J. R., A. Hikata, and C. Elbaum (1983), Sound-velocity in helium-filled porous Vycor glass, *Phys. Rev. B*, *27*, 5848–5851, doi:10.1103/PhysRevB.27.5848.

Berryman, J. G. (1980), Confirmation of Biots theory, *Appl. Phys. Lett.*, *37*, 382–384, doi:10.1063/1.91951.

Biot, M. A. (1956a), Theory of propagation of elastic waves in a fluid-saturated porous solid. 1. Low-frequency range, *J. Acoust. Soc. Am.*, *28*, 168–178, doi:10.1121/1.1908239.

Biot, M. A. (1956b), Theory of propagation of elastic waves in a fluid-saturated porous solid. 2. Higher frequency range, *J. Acoust. Soc. Am.*, *28*, 179–191, doi:10.1121/1.1908241.

Biot, M. A., and D. Willis (1957), The elastic coefficients of the theory of consolidation, *J. Appl. Mech.*, *24*, 594–601.

Bourbié, T., O. Coussy, and B. Zinszner (1987), *Acoustics of Porous Media*, Gulf, Houston, Tex.

Bouzidi, Y. (2003), *The Acoustic Reflectivity and Transmissivity of Liquid Saturated Porous Media: Experimental Tests of Theoretical Concepts*, 286 pp., Univ. of Alberta, Edmonton, Alberta, Canada.

Bouzidi, Y., and D. R. Schmitt (2006), A large ultrasonic bounded acoustic pulse transducer for acoustic transmission goniometry: Modeling and calibration, *J. Acoust. Soc. Am.*, *119*, 54–64, doi:10.1121/1.2133683.

Bouzidi, Y., and D. R. Schmitt (2008), Quantitative modeling of reflected ultrasonic bounded beams and a new estimate of the Schoch shift, *IEEE Trans. Ultrason. Ferroelectr. Frequation Control*, *55*, 2661–2673, doi:10.1109/TUFFC.2008.981.

Carcione, J. M., and H. B. Helle (2004), The physics and simulation of wave propagation at the ocean bottom, *Geophysics*, *69*, 825–839, doi:10.1190/1.1759469.

Castagnede, B., A. Aknine, M. Melon, and C. Depollier (1998), Ultrasonic characterization of the anisotropic behavior of air-saturated porous materials, *Ultrasonics*, *36*, 323–341, doi:10.1016/S0041-624X(97)00093-0.

Chandler, R. (1981), Transient streaming potential measurements on fluid-saturated porous structures—An experimental-verification of Biots slow-wave in the quasi-static limit, *J. Acoust. Soc. Am.*, *70*, 116–121, doi:10.1121/1.386689.

Chandler, R. N., and D. L. Johnson (1981), The equivalence of quasistatic flow in fluid-saturated porous-media and Biots slow-wave in the limit of zero frequency, *J. Appl. Phys.*, *52*, 3391–3395, doi:10.1063/1.329164.

Courtney, R. C., and L. Mayer (1993), Acoustic properties of fine-grained sediments from emerald basin—Toward an inversion for physical-properties using the Biot-Stoll model, *J. Acoust. Soc. Am.*, *93*, 3193–3200, doi:10.1121/1.405703.

Delacruz, V., J. Hube, and T. J. T. Spanos (1992), Reflection and transmission of seismic-waves at the boundaries of porous-media, *Wave Motion*, *16*, 323–338, doi:10.1016/0165-2125(92)90021-S.

Denneman, A. I. M., G. G. Drijkoningen, D. M. J. Smeulders, and K. Wapenaar (2002), Reflection and transmission of waves at a fluid/porous-medium interface, *Geophysics*, *67*, 282–291, doi:10.1190/1.1451800.

Deresiewicz, H., and R. Skalak (1963), On uniqueness in dynamic poroelasticity, *Bull. Seismol. Soc. Am.*, *53*, 783–788.

Derible, S. (2004), Acoustical measurement of the bulk characteristics of a water-saturated porous plate obeying Biot's theory, *Acta Acust. United Acust.*, *90*, 85–90.

Derible, S. (2005), Debye-series analysis of the transmission coefficient of a water-saturated porous plate obeying Biot's theory, *J. Acoust. Soc. Am.*, *118*, 3430–3435, doi:10.1121/1.2118248.

Diallo, M. S., and E. Appel (2000), Acoustic wave propagation in saturated porous media: Reformulation of the Biot/Squirt flow theory, *J. Appl. Geophys.*, *44*, 313–325, doi:10.1016/S0926-9851(00)00009-4.

Dutta, N. C. (1980), Theoretical analysis of observed second bulk compressional wave in a fluid-saturated porous solid at ultrasonic frequencies, *Appl. Phys. Lett.*, *37*, 898–900, doi:10.1063/1.91851.

Dvorkin, J., G. Mavko, and A. Nur (1995), Squirt flow in fully saturated rocks, *Geophysics*, *60*, 97–107, doi:10.1190/1.1443767.

Gassmann, F. (1951), Über die elastizität poröser medien, *Vierteljahrsschr. Naturforsch. Ges. Zuerich*, *96*, 1–23.

Gazdag, J. (1978), Wave equation migration with phase-shift method, *Geophysics*, *43*, 1342–1351, doi:10.1190/1.1440899.

Geerits, T. W., and O. Kelder (1997), Acoustic wave propagation through porous media: Theory and experiments, *J. Acoust. Soc. Am.*, *102*, 2495–2510, doi:10.1121/1.420304.

Gist, G. A. (1994a), Fluid effects on velocity and attenuation in sandstones, *J. Acoust. Soc. Am.*, *96*, 1158–1173, doi:10.1121/1.410389.

Gist, G. A. (1994b), Interpreting laboratory velocity measurements in partially gas-saturated rocks, *Geophysics*, *59*, 1100–1109, doi:10.1190/1.1443666.

Gomez Alvarez-Arenas, T. E., E. Riera-Franco de Sarabia, and F. R. Montero de Espinosa-Feijo (1994), Observation of a very slow ultrasonic bulk compressional wave in an inhomogeneous porous material, *Ultrasonics*, *32*, 131–140, doi:10.1016/0041-624X(94)90021-3.

Green, D. H., and H. F. Wang (1986), Fluid pressure response to undrained compression in saturated sedimentary rock, *Geophysics*, *51*, 948–956, doi:10.1190/1.1442152.

Gurevich, B., and M. Schoenberg (1999), Interface conditions for Biot's equations of poroelasticity, *J. Acoust. Soc. Am.*, *105*, 2585–2589, doi:10.1121/1.426874.

Gurevich, B., O. Kelder, and D. M. J. Smeulders (1999), Validation of the slow compressional wave in porous media: Comparison of experiments and numerical simulations, *Transp. Porous Media*, *36*, 149–160, doi:10.1023/A:1006676801197.

Haire, T. J., and C. M. Langton (1999), Biot theory: A review of its application to ultrasound propagation through cancellous bone, *Bone*, *24*, 291–295, doi:10.1016/S8756-3282(99)00011-3.

Han, D. H., and M. L. Batzle (2004), Gassmann's equation and fluid-saturation effects on seismic velocities, *Geophysics*, *69*, 398–405, doi:10.1190/1.1707059.

Hickey, C. J., and J. M. Sabatier (1997), Choosing Biot parameters for modeling water-saturated sand, *J. Acoust. Soc. Am.*, *102*, 1480–1484, doi:10.1121/1.421037.

Hickey, C. J., T. J. T. Spanos, and V. Delacruz (1995), Deformation parameters of permeable media, *Geophys. J. Int.*, *121*, 359–370, doi:10.1111/j.1365-246X.1995.tb05717.x.

Hovem, J. M. (1981), Transmission of sound through a porous disk, *Appl. Phys. Lett.*, *39*, 590–591, doi:10.1063/1.92834.

Ji, Q., L. H. Le, L. J. Filipow, and S. A. Jackson (1998), Ultrasonic wave propagation in water-saturated aluminum foams, *Ultrasonics*, *36*, 759–765, doi:10.1016/S0041-624X(97)00161-3.

Johnson, D. L. (1984), Recent developments in the acoustic properties of porous media, in *Frontiers in Physical Acoustics, Varenna on Lake Como, Villa Monastero, 10–20 July 1984*, edited by D. Sette, *Proc. Int. Sch. Phys. Enrico Fermi*, *93*, 255–290.

Johnson, D. L., and T. J. Plona (1982), Acoustic slow waves and the consolidation transition, *J. Acoust. Soc. Am.*, *72*, 556–565, doi:10.1121/1.388036.

Johnson, D. L., T. J. Plona, C. Scala, F. Pasierb, and H. Kojima (1982), Tortuosity and acoustic slow waves, *Phys. Rev. Lett.*, *49*, 1840–1844, doi:10.1103/PhysRevLett.49.1840.

Johnson, D. L., J. Koplik, and R. Dashen (1987), Theory of dynamic permeability and tortuosity in fluid-saturated porous-media, *J. Fluid Mech.*, *176*, 379–402, doi:10.1017/S0022112087000727.

Johnson, D. L., T. J. Plona, and H. Kojima (1994), Probing porous media with first and second sound. II. Acoustic properties of water-saturated porous media, *J. Appl. Phys.*, *76*, 115–125, doi:10.1063/1.358438.

Johnston, D. H., and M. N. Toksoz (1980), Thermal cracking and amplitude dependent attenuation, *J. Geophys. Res.*, *85*, 937–942, doi:10.1029/JB085iB02p00937.

Jungman, A., G. Quentin, L. Adler, and Q. Xue (1989), Elastic property measurements in fluid-filled porous materials, *J. Appl. Phys.*, *66*, 5179–5184, doi:10.1063/1.343753.

Kelder, O., and D. M. J. Smeulders (1997), Observation of the Biot slow wave in water-saturated Nivelsteiner sandstone, *Geophysics*, *62*, 1794–1796, doi:10.1190/1.1444279.

King, M. S., J. R. Marsden, and J. W. Dennis (2000), Biot dispersion for P- and S-wave velocities in partially and fully saturated sandstones, *Geophys. Prospect.*, *48*, 1075–1089, doi:10.1046/j.1365-2478.2000.00221.x.

Klimentos, T., and C. McCann (1988), Why is the Biot slow compressional wave not observed in real rocks?, *Geophysics*, *53*, 1605–1609, doi:10.1190/1.1442443.

Krebes, E. S. (1984), On the reflection and transmission of viscoelastic waves—Some numerical results, *Geophysics*, *49*, 1374–1380, doi:10.1190/1.1441765.

Kumpel, H. J. (1991), Poroelasticity—Parameters reviewed, *Geophys. J. Int.*, *105*, 783–799, doi:10.1111/j.1365-246X.1991.tb00813.x.

Kurashige, M., S. Imaida, and Y. Goto (1992), Phase velocity measurements for three bulk waves in water-saturated sintered glass beads, in *Proceedings of the International Symposium on Impact Engineering, November 2–4, 1992, Sendai, Japan*, vol. 2, edited by I. Maekawa, pp. 508–513, Int. Symp. on Impact Eng., Sendai, Japan.

Kurashige, M., T. Hayashi, and K. Imai (1999), Simulated effective elastic moduli and wave velocities in water-saturated sintered glass-beads, *Acta Mech.*, *132*, 177–194, doi:10.1007/BF01186966.

Lakes, R., H. S. Yoon, and J. L. Katz (1983), Slow compressional wave propagation in wet human and bovine cortical bone, *Science*, *220*, 513–515, doi:10.1126/science.6836296.

Mashinskii, E. I. (2006), Nonlinear amplitude–frequency characteristics of attenuation in rock under pressure, *J. Geophys. Eng.*, *3*, 291–306, doi:10.1088/1742-2132/3/4/001.

Mavko, G. M. (1979), Frictional attenuation: Inherent amplitude dependence, *J. Geophys. Res.*, *84*, 4769–4775, doi:10.1029/JB084iB09p04769.

Mavko, G., and R. Nolenhoeksema (1994), Estimating seismic velocities at ultrasonic frequencies in partially saturated rocks, *Geophysics*, *59*, 252–258, doi:10.1190/1.1443587.

Mavko, G., and A. Nur (1975), Melt squirt in asthenosphere, *J. Geophys. Res.*, *80*, 1444–1448, doi:10.1029/JB080i011p01444.

Mayr, S. I., and H. Burkhardt (2006), Ultrasonic properties of sedimentary rocks: Effect of pressure, saturation, frequency and microcracks, *Geophys. J. Int.*, *164*, 246–258, doi:10.1111/j.1365-246X.2005.02826.x.

Molyneux, J. B., and D. R. Schmitt (2000), Compressional-wave velocities in attenuating media: A laboratory physical model study, *Geophysics*, *65*, 1162–1167, doi:10.1190/1.1444809.

Nagy, P. B. (1993), Slow-wave propagation in air-filled permeable solids, *J. Acoust. Soc. Am.*, *93*, 3224–3234, doi:10.1121/1.405707.

Nagy, P. B., L. Adler, and B. P. Bonner (1990), Slow-wave propagation in air-filled porous materials and natural rocks, *Appl. Phys. Lett.*, *56*, 2504–2506, doi:10.1063/1.102872.

Nagy, P. B., B. P. Bonner, and L. Adler (1995), Slow-wave imaging of permeable rocks, *Geophys. Res. Lett.*, *22*, 1053–1056, doi:10.1029/95GL00906.

Nakagawa, K., K. Soga, and J. K. Mitchell (1997), Observation of Biot compressional wave of the second kind in granular soils, *Geotechnique*, *47*, 133–147.

O'Connell, R. J., and B. Budiansky (1974), Seismic velocities in dry and saturated cracked solids, *J. Geophys. Res.*, *79*, 5412–5426, doi:10.1029/JB079i035p05412.

Ogushwitz, P. R. (1985), Applicability of the Biot theory. I. Low-porosity materials, *J. Acoust. Soc. Am.*, *77*, 429–440, doi:10.1121/1.391863.

Plona, T. J. (1980), Observation of a second bulk compressional wave in a porous medium at ultrasonic frequencies, *Appl. Phys. Lett.*, *36*, 259–261, doi:10.1063/1.91445.

Pride, S. R., E. Tromeur, and J. G. Berryman (2002), Biot slow-wave effects in stratified rock, *Geophysics*, *67*, 271–281, doi:10.1190/1.1451799.

Rasolofosaon, P. N. J. (1988), Importance of interface hydraulic condition on the generation of second bulk compressional wave in porous media, *Appl. Phys. Lett.*, *52*, 780–782, doi:10.1063/1.99282.

Rubino, J. G., C. L. Ravazzoli, and J. E. Santos (2006), Reflection and transmission of waves in composite porous media: A quantification of energy conversions involving slow waves, *J. Acoust. Soc. Am.*, *120*, 2425–2436, doi:10.1121/1.2354464.

Santos, J. E., J. M. Corbero, C. L. Ravazzoli, and J. L. Hensley (1992), Reflection and transmission coefficients in fluid-saturated porous-media, *J. Acoust. Soc. Am.*, *91*, 1911–1923, doi:10.1121/1.403702.

Sebaa, N., Z. E. A. Fellah, M. Fellah, E. Ogam, A. Wirgin, F. G. Mitri, C. Depollier, and W. Lauriks (2006), Ultrasonic characterization of human cancellous bone using the Biot theory: Inverse problem, *J. Acoust. Soc. Am.*, *120*, 1816–1824, doi:10.1121/1.2335420.

Sen, P. N., C. Scala, and M. H. Cohen (1981), A self-similar model for sedimentary-rocks with application to the dielectric-constant of fused glass-beads, *Geophysics*, *46*, 781–795, doi:10.1190/1.1441215.

Smeulders, D. M. J. (2005), Experimental evidence for slow compressional waves, *J. Eng. Mech.*, *131*, 908–917, doi:10.1061/(ASCE)0733-9399(2005)131:9(908).

Stearns, R. G. (1992), Measurement of a multicomponent granular system using acoustic slow waves, *J. Appl. Phys.*, *71*, 606–611, doi:10.1063/1.350413.

Stoll, R. D. (1989), *Sediment Acoustics*, Springer, New York.

Stoll, R. D., and T. K. Kan (1981), Reflection of acoustic waves at a water-sediment interface, *J. Acoust. Soc. Am.*, *70*, 149–156, doi:10.1121/1.386692.

Tajuddin, M., and S. J. Hussaini (2005), Reflection of plane waves at boundaries of a liquid filled poroelastic half-space, *J. Appl. Geophys.*, *58*, 59–86, doi:10.1016/j.jappgeo.2005.04.003.

Thomsen, L. (1985), Biot-consistent elastic moduli of porous rocks: Low-frequency limit, *Geophysics*, *50*, 2797–2807, doi:10.1190/1.1441900.

Watson, J. T. R., R. S. Basu, and J. V. Sengers (1980), An improved representative equation for the dynamic viscosity of water substance, *J. Phys. Chem. Ref. Data*, *9*, 1255–1290.

Williams, K. L., D. R. Jackson, E. I. Thorsos, D. J. Tang, and S. G. Schock (2002), Comparison of sound speed and attenuation measured in a sandy sediment to predictions based on the Biot theory of porous media, *IEEE J. Oceanic Eng.*, *27*, 413–428, doi:10.1109/JOE.2002.1040928.

Wu, K. Y., Q. Xue, and L. Adler (1990), Reflection and transmission of elastic waves from a fluid-saturated porous solid boundary, *J. Acoust. Soc. Am.*, *87*, 2349–2358, doi:10.1121/1.399081.

Yang, J. (1999), Importance of flow condition on seismic waves at a saturated porous solid boundary, *J. Sound Vibrat.*, *221*, 391–413, doi:10.1006/jsvi.1998.2036.

Yang, J., and T. Sato (1998), Influence of viscous coupling on seismic reflection and transmission in saturated porous media, *Bull. Seismol. Soc. Am.*, *88*, 1289–1299.

Zhu, G. Z., X. F. Zhu, and L. Liu (1999), Examination of the existence of slow wave in fluid saturated porous medium with the optical method, *Chin. J. Acoust.*, *18*, 304–310.

Y. Bouzidi, Divestco Processing, Divestco Inc., Suite 500, 440 2nd Avenue S.W., Calgary, AB T2P 5A9, Canada.

D. R. Schmitt, Institute for Geophysical Research, Department of Physics, University of Alberta, Edmonton, AB T6G 2G7, Canada. (doug@phys.ualberta.ca)